


Article

Development of a Parallel Dual-Stage Compliant Nanopositioning System

Xu Yang ¹, Lichao Ji ¹, Ying Shang ², Wule Zhu ³ and Shizhen Li ^{1,*} 

¹ Institute of Marine Science and Technology, Shandong University, Qingdao 266237, China; xu_y@sdu.edu.cn (X.Y.); 202016936@mail.sdu.edu.cn (L.J.)

² Laser Institute, Qilu University of Technology, Jinan 250353, China; shangying@sdlaser.cn

³ State Key Laboratory of Fluid Power and Mechatronic Systems, Zhejiang University, Hangzhou 310027, China; wulezhu@zju.edu.cn

* Correspondence: lishizhen@sdu.edu.cn

Abstract: This paper presents a novel parallel dual-stage compliant nanopositioning system (PDCNS), aimed at nanoscale positioning for microscale manipulation. In the developed PDCNS, the coarse stage actuated by the voice coil motor and the fine stage driven by the piezoelectric actuator are integrated in a parallel manner by a specially devised A-shaped compliant mechanism, which leads to many excellent performances, such as good resolution and large stroke and broadband. To enhance the closed-loop-positioning capability of the proposed PDCNS, a double-servo cooperative control (DSCC) strategy is specially constructed. The performance of the proposed PDCNS is evaluated by analytical model, finite element analysis, and experimental research. Results show that the first-order resonance frequency of the designed A-shaped compliant mechanism can reach 99.7 Hz. Combined with the designed DSCC, the developed PDCNS prototype is demonstrated to provide a stroke of 1.49 mm and a positioning resolution of ≤ 50 nm.

Keywords: nanopositioning system; microscale manipulation; compliant mechanism; double-servo cooperative control



Citation: Yang, X.; Ji, L.; Shang, Y.; Zhu, W.; Li, S. Development of a Parallel Dual-Stage Compliant Nanopositioning System. *Actuators* **2022**, *11*, 136. <https://doi.org/10.3390/act11050136>

Academic Editors: Nicola Pio Belfiore and Jose Luis Sanchez-Rojas

Received: 19 March 2022

Accepted: 9 May 2022

Published: 13 May 2022

Publisher's Note: MDPI stays neutral with regard to jurisdictional claims in published maps and institutional affiliations.



Copyright: © 2022 by the authors. Licensee MDPI, Basel, Switzerland. This article is an open access article distributed under the terms and conditions of the Creative Commons Attribution (CC BY) license (<https://creativecommons.org/licenses/by/4.0/>).

1. Introduction

Precision-positioning platforms with nanometer resolution play more and more important roles in many scientific and industrial applications [1–6]. In previous research, piezoelectric actuators were often adopted to configure these nanopositioning stages because of their fast speed and nanometer-level resolution [7–10]. Nevertheless, the maximum stroke of the piezoelectric actuator is only about 0.1% of its length [11]. Piezoelectric motors which can realize continuous nanoscale movement without stroke limit have been applied in nanopositioning systems as well [12–15]. However, the piezoelectric motors encounter severe nonlinear friction. To overcome these drawbacks, the dual-stage nanopositioning systems are employed to deliver high-resolution motion over a long range.

In the literature, some types of dual-stage positioning systems were proposed. To improve the areal density of the magnetic hard disk, a dual-stage positioning mechanism was designed to regulate the position of read–write head, in which an additional piezoelectric actuator was mounted on the primary stage for fast and fine positioning [16]. Fast tool servo units based on the piezoelectric actuator or electromagnetic actuator were used to cooperate with the feed shaft of machine tools for high-speed and high-accuracy nanocutting [17–19]. A piezo-driven compliant injector was configured at the terminal of a traditional XYZ-positioning stage to accomplish the automatic injection and batch micromanipulation of cells [20,21]. However, the previous design concepts of the dual-stage system were limited to stacking a fine stage on top of a coarse stage in a serial manner, which encountered many technical bottlenecks, such as large moving mass, assembly error,

and uncertain disturbance from the cable. Therefore, new configurations of dual-stage positioning systems are still required.

Apart from the structure design, the control strategy also significantly influences the performance of the dual-stage positioning system. Extensive research on the closed-loop control of the dual-stage positioning system was carried out in the past few years. For example, Xu et al. [22] and Michellod et al. [23] designed single-feedback control schemes for the dual-stage nanopositioning system that determines the relative position between two stages using observers. By employing the position feedbacks from coarse and fine stages, Dong et al. [24] and Zhu et al. [25] proposed multiple-feedback control systems for the dual-stage nanopositioning system. Despite this, it is still a challenging job to control a dual-stage positioning system.

In this paper, a novel parallel dual-stage compliant nanopositioning system (PDCNS) with a corresponding double-servo cooperative control (DSCC) strategy is developed. The PDCNS employs a new A-shaped compliant parallel mechanism to combine the coarse motion from the voice coil motor and the fine motion from the piezoelectric actuator. Considering the uncertain disturbances and the double-input-single-output configuration, a DSCC is designed in this paper to enhance the motion capability of the proposed PDCNS. The static and dynamic performances of the PDCNS are investigated by the analytical-model-based calculation and the finite element analysis. Moreover, a series of experimental studies are carried out to demonstrate the kinematic properties and closed-loop-positioning performance of the PDCNS.

The rest of this paper is organized as follows: Section 2 presents the mechanical design of the PDCNS. An analytical model of the PDCNS is established in Section 3. With the analytical model and finite element analysis, the static and dynamic performances of the proposed PDCNS are analyzed in Section 4. Moreover, experiments are conducted to evaluate the static and dynamic performances of the proposed PDCNS in Section 5. Finally, conclusions are given in Section 6.

2. Design of PDCNS

The PDCNS consists of an A-shaped compliant parallel mechanism (ACPM), a voice coil motor and a piezoelectric actuator, as shown in Figure 1. The ACPM can transmit the motion of the voice coil motor (VCM) to the end effector through two parallel limbs. At the same time, the piezoelectric actuator (PEA) contributes to the motion of the end effector via a half bridge-type compliant chain. For compactness, the upper part of the ACPM and the half bridge-type chain share the same flexural structure. To eliminate parasitic motions, two guiding flexible beams are designed for the end effector which help to improve the resonant frequency as well. In addition, two input decoupling compliant mechanisms are devised to protect the piezoelectric actuator from undesired lateral forces. A support bearing is adopted to guide the actuation motion of the voice coil motor.

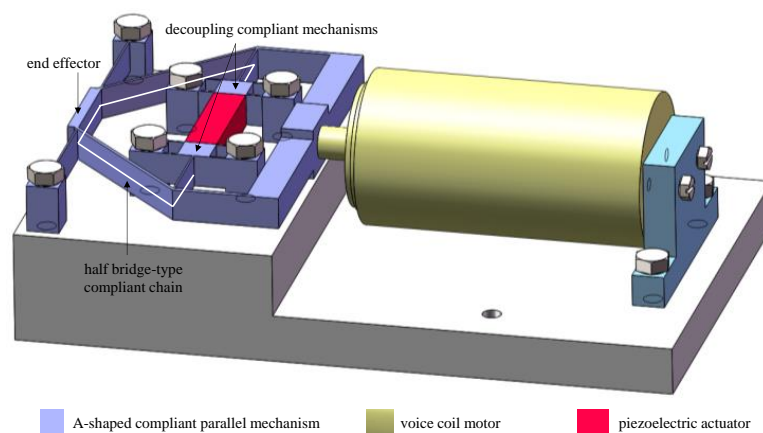


Figure 1. Structure of the PDCNS.

With the above designs, both the voice coil motor and the piezoelectric actuator can contribute to the output motion. As the voice coil motor has a large-range motion capability and the piezoelectric actuator features a high-resolution motion characteristic, the proposed PDCNS is expected to position in the millimeter range with nanometer resolution. Moreover, as the bases of the voice coil motor and the piezoelectric actuator remain static to the ground, low-moving mass and high dynamics can be realized.

3. Analytical Modelling

In this section, the kinematic and stiffness characteristics of PDCNS are investigated. Based on the finite element theory [26,27], an analytical model is built for the ACPM, as shown in Figure 2. We can see from the figure, rigid nodes with three degrees of freedom are defined at the two ends of the beams to describe the deformation of the flexible beam. A global coordinate system $O-xy$ is defined to analyze the overall deformation of ACPM.

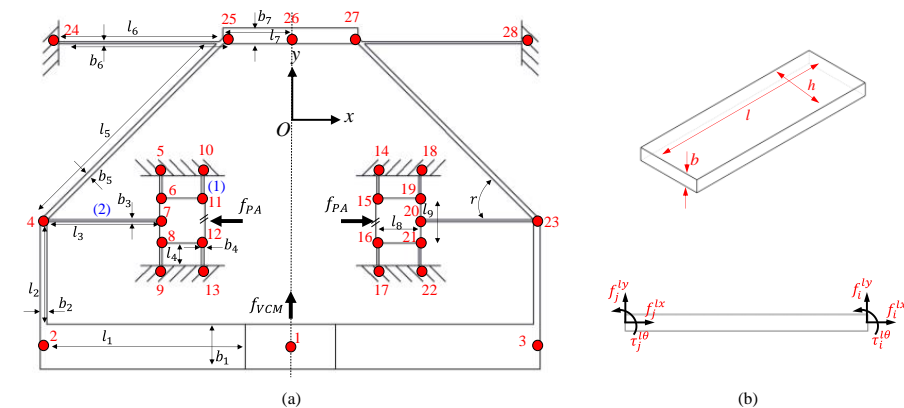


Figure 2. (a) Analytical model of ACPM, (b) schematic of flexible beam.

According to the structural mechanics theory [26,28], in the local coordinate system of the flexible beam, the relationship between the applied force and the induced displacement of the flexible beam can be expressed as

$$\begin{bmatrix} f_i^{lx} \\ f_i^{ly} \\ \tau_i^{l\theta} \\ f_j^{lx} \\ f_j^{ly} \\ \tau_j^{l\theta} \end{bmatrix} = \begin{bmatrix} \frac{Ebh}{l} & 0 & 0 & -\frac{Ebh}{l} & 0 & 0 \\ 0 & \frac{12EI}{l^3} & \frac{6EI}{l^2} & 0 & -\frac{12EI}{l^3} & \frac{6EI}{l^2} \\ 0 & \frac{6EI}{l^2} & \frac{4EI}{l} & 0 & -\frac{6EI}{l^2} & \frac{2EI}{l} \\ -\frac{Ebh}{l} & 0 & 0 & \frac{Ebh}{l} & 0 & 0 \\ 0 & -\frac{12EI}{l^3} & -\frac{6EI}{l^2} & 0 & \frac{12EI}{l^3} & -\frac{6EI}{l^2} \\ 0 & \frac{6EI}{l^2} & \frac{2EI}{l} & 0 & -\frac{6EI}{l^2} & \frac{4EI}{l} \end{bmatrix} \begin{bmatrix} \delta_i^{lx} \\ \delta_i^{ly} \\ \phi_i^{l\theta} \\ \delta_j^{lx} \\ \delta_j^{ly} \\ \phi_j^{l\theta} \end{bmatrix} = k_{loc} \begin{bmatrix} \delta_i^{lx} \\ \delta_i^{ly} \\ \phi_i^{l\theta} \\ \delta_j^{lx} \\ \delta_j^{ly} \\ \phi_j^{l\theta} \end{bmatrix} \quad (1)$$

where $f_i^{lx}, f_i^{ly}, \tau_i^{l\theta}$ are the x -, y -directional forces and z -directional torque applied on node i in the local coordinate system, $f_j^{lx}, f_j^{ly}, \tau_j^{l\theta}$ are the x -, y -directional forces and z -directional torque applied on node j in the local coordinate system, $\delta_i^{lx}, \delta_i^{ly}, \phi_i^{l\theta}$ are the x -, y -directional translations and z -directional angular displacement of node i in the local coordinate system, $\delta_j^{lx}, \delta_j^{ly}, \phi_j^{l\theta}$ are the x -, y -directional translations and z -directional angular displacement of node j in the local coordinate system, E is Young's modulus, b, h are the section sizes of the flexible beam, l is the length of the flexible beam, and I is the moment of inertia of the flexible beam which can be calculated by $I = hb^3/12$, k_{loc} is the local stiffness matrix of the flexible beam.

With Equation (1), the loads applied on the two end ports of the flexible beam can be calculated according to the displacements of the corresponding two rigid nodes. Nevertheless, the stiffness matrix in Equation (1) is expressed in the local coordinate system, which relates the deformations and loads of the flexible beam in the local coordinate system. To combine the deformations and loads of all the flexible beams, a rotation transformation is

employed to transfer the local stiffness matrix, k_{loc} , to be a global stiffness matrix, k_{glo} , as shown in Equation (3) [26,29].

$$R(\theta) = \begin{bmatrix} \cos(\theta) & \sin(\theta) & 0 & 0 & 0 & 0 \\ -\sin(\theta) & \cos(\theta) & 0 & 0 & 0 & 0 \\ 0 & 0 & 1 & 0 & 0 & 0 \\ 0 & 0 & 0 & \cos(\theta) & \sin(\theta) & 0 \\ 0 & 0 & 0 & -\sin(\theta) & \cos(\theta) & 0 \\ 0 & 0 & 0 & 0 & 0 & 1 \end{bmatrix} \quad (2)$$

$$k_{glo} = R(\theta) \cdot k_{loc} \cdot R(\theta)^T \quad (3)$$

where $R(\theta)$ is the rotation matrix, θ is the angle between the local and global coordinate systems (defined as the angle from the x axis of the local coordinate system to the x axis of the global coordinate system around the o point of the local coordinate system).

With the global stiffness matrix in (3) and the analytical model in Figure 2a, an overall stiffness matrix, K , can be established for the ACPM with the finite element theory [26,30], which is able to depict the relationship between the external forces and induced deformations as follows.

$$\begin{bmatrix} f_1^x & f_1^y & \tau_1^\theta & \cdots & f_{28}^x & f_{28}^y & \tau_{28}^\theta \end{bmatrix}^T = K \cdot \begin{bmatrix} \delta_1^x & \delta_1^y & \phi_1^\theta & \cdots & \delta_{28}^x & \delta_{28}^y & \phi_{28}^\theta \end{bmatrix}^T \quad (4)$$

where f_i^x and f_i^y are the x - and y -directional external forces applied on node i , τ_i^θ is the external torque around the z -axis applied on node i , δ_i^x , and δ_i^y are the x - and y -directional translations of node i , and ϕ_i^θ is the rotational angle (around z -axis) of node i .

While two input forces, f_{PA} , are applied on nodes 7 and 20, the resulting input displacements, δ_1^y , from static equilibrium Equation (4) can be set to zero (unchanged with respect to the ground) by searching for a suitable actuation force, f_{VCM} , for node 1. Under the above conditions, the input displacements, δ_7^x and δ_{20}^x , as well as the output displacement, δ_{26}^y , can be calculated.

(1) The input stiffness for the PEA can be derived as:

$$k_{in}^{PEA} = \frac{f_{PA}}{|\delta_7^x| + |\delta_{20}^x|} \quad (5)$$

(2) The displacement amplification ratio for the PEA can be derived as:

$$\lambda_{amp}^{PEA} = \frac{|\delta_{26}^y|}{|\delta_7^x| + |\delta_{20}^x|} \quad (6)$$

(3) The maximum stress coefficient of the beam 1 contributed by the input displacement of PEA can be calculated by [30,31].

$$\xi_{11} = \frac{3 \cdot k_c \cdot E \cdot b_4 \cdot |\delta_{11}^x|}{2 \cdot l_4^2 \cdot (|\delta_7^x| + |\delta_{20}^x|)} \quad (7)$$

where k_c is the stress concentration factor which is set to 2 in this paper.

By applying one input force, f_{VCM} , on node 1 and in the meantime imposing a suitable actuation force, f_{PA} , on nodes 7 and 20, the resulting input displacement $|\delta_7^x| + |\delta_{20}^x|$ from static equilibrium Equation (4) can be set to zero. Under the above conditions, the induced input displacement, δ_1^y , and output displacement, δ_{26}^y , can be calculated.

(4) The input stiffness for the VCM can be derived as:

$$k_{in}^{VCM} = \frac{f_{VCM}}{|\delta_1^y|} \quad (8)$$

(5) The displacement amplification ratio for the VCM can be derived as:

$$\lambda_{amp}^{VCM} = \frac{|\delta_{26}^y|}{|\delta_1^y|} \quad (9)$$

(6) The maximum stress coefficient of beam 2 contributed by the input displacement of the VCM can be calculated by [30,31].

$$\xi_{22} = \frac{3 \cdot k_c \cdot E \cdot b_3 \cdot |\delta_4^y|}{2 \cdot l_3^2 \cdot |\delta_1^y|} \quad (10)$$

(7) For the PDCNS, the maximum stress usually occurs in beam 1 or beam 2. Hence, a maximum stress matrix is established for the PDCNS as follows:

$$\begin{bmatrix} \sigma_{max}^1 \\ \sigma_{max}^2 \end{bmatrix} = \begin{bmatrix} \xi_{11} & 0 \\ 0 & \xi_{22} \end{bmatrix} \begin{bmatrix} |\delta_7^x| + |\delta_{20}^x| \\ |\delta_1^y| \end{bmatrix} \quad (11)$$

where σ_{max}^1 and σ_{max}^2 are the maximum stresses of beam 1 and beam 2, respectively. According to (11), the compressive stress of beam 2 induced by the PEA is ignored since it is small compared to the bending stress induced by the maximum displacement of the VCM. Due to the good input decoupling, the bending stress of beam 1 induced by the VCM is ignored as well.

4. Simulation Analysis

Based on the working principles of the PDCNS, a 3D virtual prototype is built by using the SOLIDWORKS software. The kinematic and stiffness performances of the PDCNS virtual prototype are evaluated by the established analytical model. The key parameters of the analytical model are listed in Table 1. The dimensions of the PDCNS virtual prototype are indicated in Figure 2. The material utilized for analysis is TC4 titanium alloy with Young's modulus E , Poisson's ratio μ , and mass density ρ [32,33]. To validate the static and dynamic performances of the PDCNS virtual prototype, ANSYS Workbench-based FEA simulation is carried out as well in this section. The computational models for FEA analysis are configured as follows: mesh physics preference = mechanical, mesh size function = proximity and curvature, mesh relevance = -75 , inner surfaces of six bolt holes is fixed, solver type = program controlled.

Table 1. Key parameters for simulation.

l_1 mm	b_1 mm	l_2 mm	b_2 mm	l_3 mm	b_3 mm	l_4 mm	b_4 mm	l_5 mm	b_5 mm	l_6 mm
43.98	10	22.75	1.5	25	0.5	5	0.5	55.13	1	35
b_6 mm	l_7 mm	b_7 mm	l_8 mm	l_9 mm	r °	$w_i (i = 1 \sim 7)$ mm	E $\times 10^{11}$ Pa	μ	ρ kg/m ³	
0.5	15	3.5	10	10	45°	10	1.167	0.36	4414	

First, by applying a driving force (38.36 N) to the input end of the VCM and fixing the input end of the PEA in the ANSYS Workbench, the resulting overall deformation of the proposed ACPM can be obtained as shown in Figure 3a. The slight displacement difference between the two input ends of PEA can be attributed to asymmetric probe location, asymmetric mesh generation, computational convergence error, etc. The displacement amplification ratio for the VCM can be derived by relating the displacements of the VCM and the end effector. The input stiffness for VCM can be revealed by identifying the slope of

the applied force over the induced displacement. As seen in Table 2, the amplification ratio for the VCM is approximately 1, which means that the motion of the VCM is transmitted to the end effector almost directly. The input stiffness for the VCM is revealed to be only 0.026 N/ μm , which helps to achieve a large stroke. Good agreement between the results of the analytical model and the ANSYS Workbench are obtained, confirming the performance of the proposed ACPM.

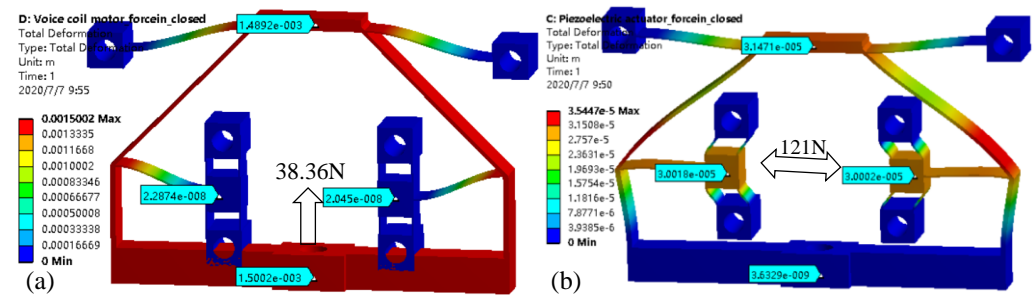


Figure 3. Displacement distribution of ACPM while (a) actuating the input end of VCM with 38.36 N and fixing the input end of PEA, (b) driving the input end of PEA with 121 N and fixing the input end of VCM.

Table 2. Performance of the ACPM virtual prototype.

	Amplification Ratio		Input Stiffness (N/ μm)		Stress Coefficient (Mpa/ μm)	
	λ_{amp}^{PEA}	λ_{amp}^{VCM}	k_{in}^{PEA}	k_{in}^{VCM}	ξ_{11}	ξ_{22}
anal.	0.514	0.997	2.41	0.0249	3.49	0.279
ANSYS	0.524	0.993	2.02	0.0256	3.11	0.287

Similarly, by applying a driving force of 121 N to the input ends of the PEA and fixing the input end of the VCM in the ANSYS Workbench, the resulting deformation of the proposed ACPM is shown in Figure 3b. The amplification ratio and input stiffness for the PEA are revealed to be 0.52 and 2.02 N/ μm , respectively, which are highly consistent with the analytical predictions, as shown in Table 2.

Corresponding to the deformations shown in Figure 3, the stress distributions of ACPM are also resolved in the ANSYS Workbench, as illustrated in Figure 4. It can be observed that the beam between nodes 20 and 23 (which has the same stress state as beam 2) is revealed to have the maximum stress, while the VCM is working at its maximum stroke of 1.5 mm. The beam between nodes 16 and 17 (which has the same stress state as beam 1) tends to show the maximum stress, while the PEA is working at the displacement of 60 μm . The obtained maximum stress coefficients are tabulated in Table 2, which agree well with the analytical results.

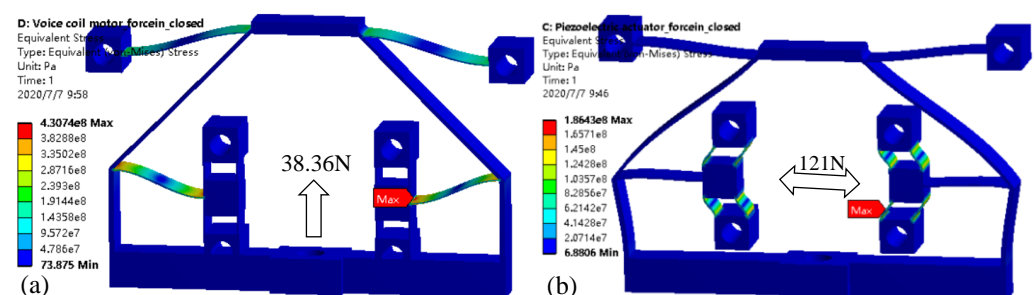


Figure 4. Stress distribution of ACPM while (a) actuating the input end of VCM with 38.36 N and fixing the input end of PEA, (b) driving the input end of PEA with 121 N and fixing the input end of VCM.

To reveal the maximum stress while the proposed ACPM is actuated by the VCM and PEA simultaneously, two actuation displacements of 1.5 mm ($|\delta_1^y|$) and 60 μm ($|\delta_7^x| + |\delta_{20}^x|$) are applied on the ACPM, as shown in Figure 5. It can be observed that beam 2 shows the maximum stress with a value close to the maximum stress shown in Figure 4a. Furthermore, the maximum stresses of the node16-node17 beams (beam between nodes 16 and 17) in Figures 4b and 5 are close to each other. Therefore, for the proposed ACPM, the maximum stress of beam 2 is mainly contributed by the VCM. Because of the input-decoupling compliant mechanisms, the VCM has limited influence on the stress of beam 1.

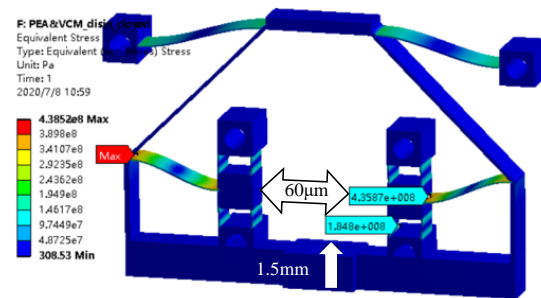


Figure 5. Stress distribution of ACPM while actuating VCM and PEA simultaneously.

Finally, modal analysis of the proposed ACPM is carried out in the ANSYS Workbench software. Considering the guiding function of the bearing of the VCM, a cylindrical support with the Y-translational freedom is applied on the input end of the VCM. Undesired out-of-plane resonances can be attenuated by the VCM bearing. Figure 6 shows the revealed first-order modal shape of the proposed ACPM. It can be seen that the first resonant resonance occurs along the actuation direction of the VCM with a frequency of 99.7 Hz. Therefore, while in open-loop control mode, the VCM actuation should be operated below 99.7 Hz to avoid mechanical resonance.

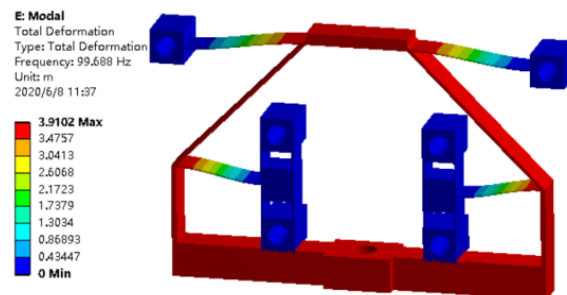


Figure 6. First modal shape of ACPM.

5. Experimental Analysis

A PDCNS prototype is fabricated to verify its kinematic performance as well as study its closed-loop motion capability, as shown in Figure 7. The ACPM with the dimensions shown in Table 1 is monolithically fabricated from TC4 titanium alloy. A commercial VCM (TM motion, model: TMEH0250, with a support bearing) and a commercial PEA (model: NAC2015-H38, maximum displacement: 59.4 μm , maximum thrust: 4200 N) are adopted to actuate the ACPM. To evaluate the motion of the ACPM, two laser displacement sensors (KEYENCE, model: LK-G10, max. measurement range: ± 1) mm are used to measure the displacements of the VCM and the end effector, and two capacitance displacement sensors (MTI Instruments, model: ASP-125M, max. measurement range: 125 μm) are employed to detect the input displacement of the PEA. The following experiments are carried out on a PC with a PCI-6259 data acquisition card.

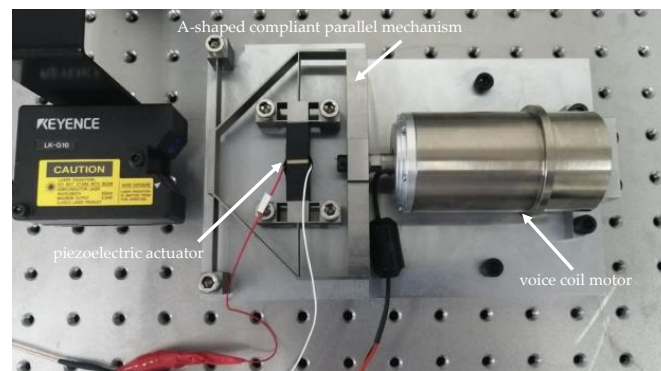


Figure 7. Experimental setup of PDCNS prototype.

5.1. Kinematic Investigation

The displacement amplification ratio for the VCM is identified by maintaining the position of the PEA with a closed-loop control and increasing the control signal of the VCM at the same time. Figure 8a shows the obtained displacement relationship between the end effector and the VCM while the displacement of the PEA is maintained at 0 μm . The displacement amplification ratio for the VCM is calculated to be 0.992. The small difference between the measured and calculated displacement amplification ratios of VCM confirms the effectiveness of the established analytical model.

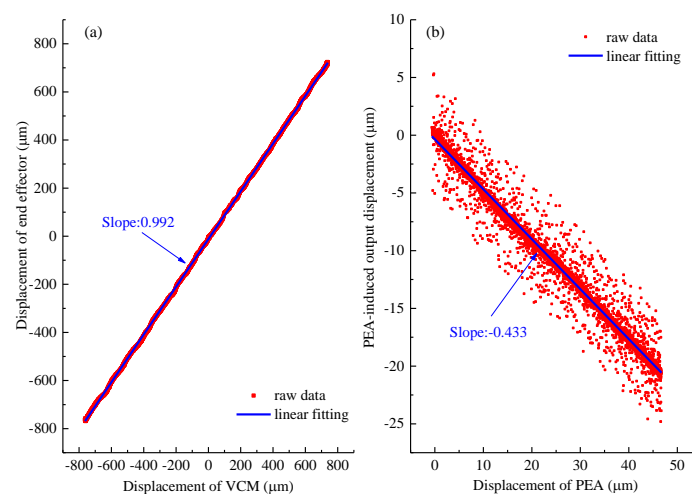


Figure 8. Kinematic test: (a) the displacement relationship between VCM and end effector while the displacement of the PEA is maintained at 0 μm , and (b) the relationship between the PEA displacement and the PEA-induced output displacement.

By applying a triangular-waveform signal with a frequency of 0.1 Hz and amplitude of 5 V to the PEA (maintaining the control voltage of the VCM at 0 V), the induced displacement of the end effector and the coupling displacement of the VCM are measured and recorded. By calculating the output displacement induced by the VCM (product of the identified amplification ratio and measured displacement of the VCM) and subtracting it from the measured displacement of the end effector, the PEA-induced output displacement can be obtained. Figure 8b shows the measured relationship between the displacement of PEA and the output displacement induced by PEA. Because of measurement noise, the measured raw data are distributed around the linear fitting line. Despite this, the kinematic of the PEA actuation can be identified according to the slope ratio of fitted linear line. The displacement amplification ratio for PEA is obtained to be 0.433. According to the established analytical model, the amplification ratio for the PEA is 0.514. By means of finite element analysis (based on ANSYS Workbench), the amplification ratio for the PEA is

evaluated to be 0.524. The deviation between the proposed method and the finite element analysis is only 2.0%. Nevertheless, the deviation between the proposed method and the experiments is 15.7%. This obvious deviation of the PEA displacement amplification ratio can be attributed to manufacturing error, assembly error, mismatched material parameters, etc.

5.2. Stroke and Hysteresis Investigation

The stroke and hysteresis characteristics of the proposed PDCNS are further investigated. First, two 0.1 Hz triangular control signals with amplitudes of 10 V and 5 V are separately applied to the VCM. The displacement responses of the PDCNS are obtained, as in Figure 9a. It can be seen that the maximum stroke of the PDCNS can reach 1.49 mm. While the output displacement of PDCNS is calibrated to be 1.49 mm, the maximum stress of the ACPM is simulated to be 431 Mpa, which is below the yield stress of TC4 titanium alloy (>790 Mpa [32]), as shown in Figures 3a and 4a. Hence, the stroke of the PDCNS prototype is limited by the maximum driving force of the voice coil motor. Besides, due to the friction of the VCM's bearing, a significant dead zone exists in the response curve of PDCNS. Then, another two triangular control signals are applied to the PEA, as illustrated in Figure 9b. Compared to the VCM-actuated PDCNS, the PEA-actuated PDCNS is free of the friction-induced dead zone. In the meantime, the PEA-actuated PDCNS displays a reduced hysteresis behavior.

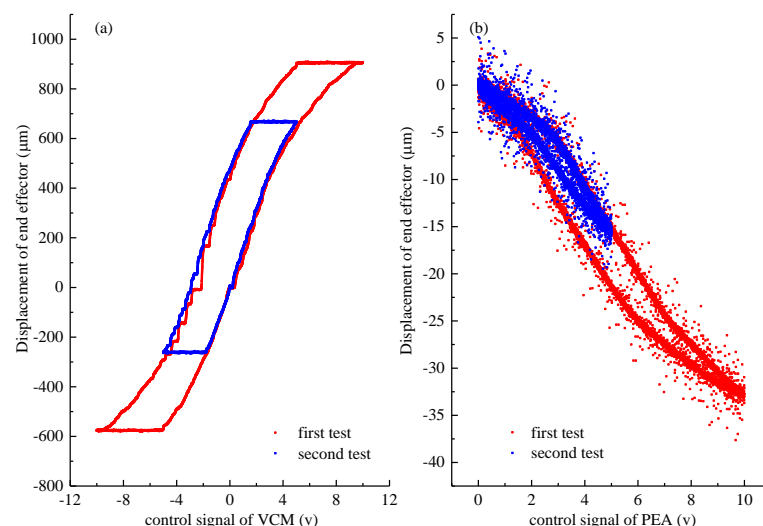


Figure 9. Stroke and hysteresis tests: (a) relationship between the displacement of the end effector and the control voltage of the VCM, (b) relationship between the displacement of the end effector and the control voltage of the PEA.

5.3. Motion Resolution Investigation

Consecutive-step-positioning experiments are carried out to investigate the motion resolution of the proposed PDCNS, as shown in Figure 10. A clear motion resolution with a step size of $0.74 \mu\text{m}$ can be achieved while the PDCNS is actuated by PEA, which is mainly limited by the resolution of the displacement sensor. Compared to the PEA-actuated PDCNS, the VCM-actuated PDCNS exhibits a much worse resolution with an average step size of $9.04 \mu\text{m}$. The unstable response of the VCM-actuated PDCNS can be attributed to the nonlinearity and friction effects. Hence, the PEA-actuated PDCNS possesses an obvious advantage in high-resolution motion.

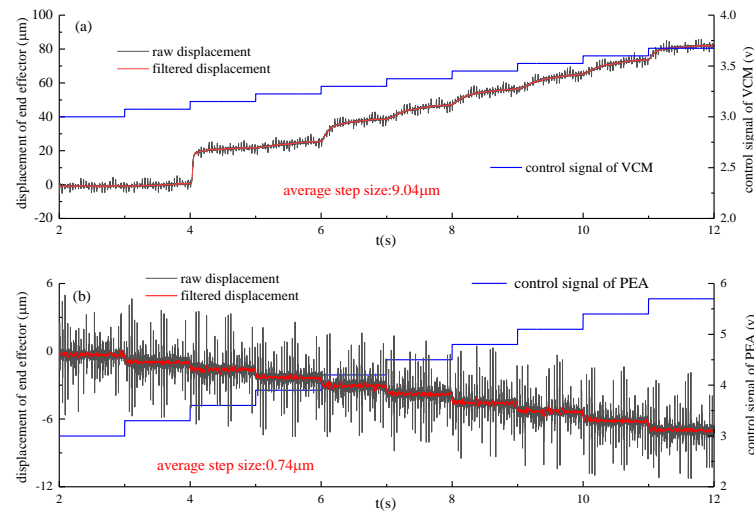


Figure 10. Motion responses with consecutive step control signals applied on (a) VCM, (b) PEA.

5.4. Closed-Loop Motion Investigation

(1) DSCC Design. Considering that the proposed PDCNS is a two-inputs-one-output system with severe hysteresis nonlinearity, a double-servo cooperative control (DSCC) strategy is designed in this section. Figure 11 depicts the block diagram of the proposed DSCC. The DSCC consists of three main parts: position observer, VCM servo control, and PEA servo control. The position observer is designed to estimate the virtual center of the end effector, x^{vir} , (the position of the end effector if the control voltage of PEA is zero) according to the displacement feedback of end effector as follows: the output displacement induced by PEA is calculated by multiplying the control voltage, V_{PEA} , and the voltage-displacement coefficient, γ_{PEA} ; by removing the PEA-induced displacement from the measured position (with the laser displacement sensor) of the end effector, the virtual center of the end effector can be obtained. Using the virtual center of the end effector as feedback, a PID-based servo control strategy with adaptive parameters is designed to control the VCM according to the reference position, x^{ref} . The VCM servo control can not only converge the end effector to the reference position with coarse resolution but also ensure that the PEA is working within its rated range. To cooperate with the VCM actuation, a PID-based PEA servo control method is employed to achieve the fine motion and assure the position accuracy. Additionally, an initial 5 V is added to the control voltage of PEA, V_{PEA} , to ensure that the output signal of PEA servo control, V_{PEA} , can be regulated within $-5\text{ V} \sim +5\text{ V}$ (the control voltage range of PEA driver is $0 \sim 10\text{ V}$). With the specially designed DSCC, the PDCNS is expected to realize nm-level positioning over mm-level range.

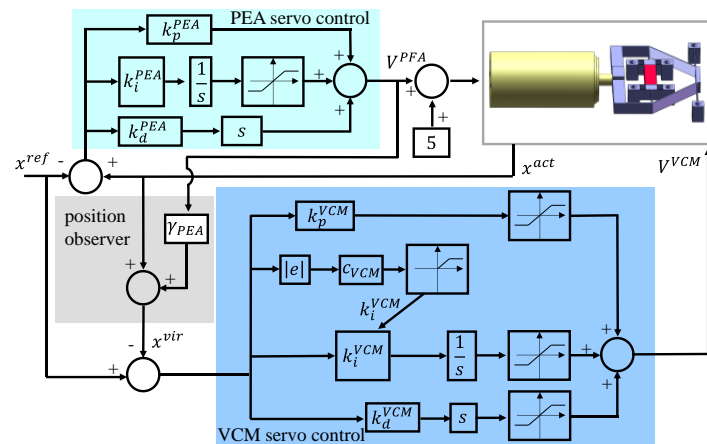


Figure 11. Block diagram of the double-servo cooperative control (DSCC) strategy.

(2) Positioning in mm-level range. A consecutive-step reference trajectory is adopted to guide the PDCNS (with DSCC) from -0.7 mm to 0.65 mm. For comparison, the VCM (with traditional PID) positioning experiments are also conducted based on the PDCNS prototype (while the control voltage of PEA is maintained at zero). The parameters of the PDCNS positioning (cooperation of voice coil motor and piezoelectric actuator) are tuned to be: VCM proportional coefficient = 0.03 , VCM integral coefficient is adaptive, VCM derivative coefficient = 1×10^{-4} , voltage-displacement coefficient = 2.5 , PEA proportional coefficient = 0.2 , PEA integral coefficient = 150 , and PEA derivative coefficient = 1×10^{-5} . In contrast, the parameters of the VCM positioning (only using the voice coil motor) are tuned to be: VCM proportional coefficient = 0.03 , VCM integral coefficient = 0.3 , and VCM derivative coefficient = 1×10^{-4} . The trajectory control results of the PDCNS (with DSCC) and the VCM (with PID) are compared in Figure 12. It can be observed that both PDCNS and VCM are effective for the mm-level positioning. Compared to the VCM, the PDCNS can realize a faster response and eliminate the steady-state error. Due to the fast response, PDCNS also induces an obvious overshoot. Figure 13 depicts the motion-tracking experiments of VCM and PDCNS while facing a consecutive-step trajectory from 0.7 mm to -0.65 mm, which confirms the global-positioning capability of the PDCNS.

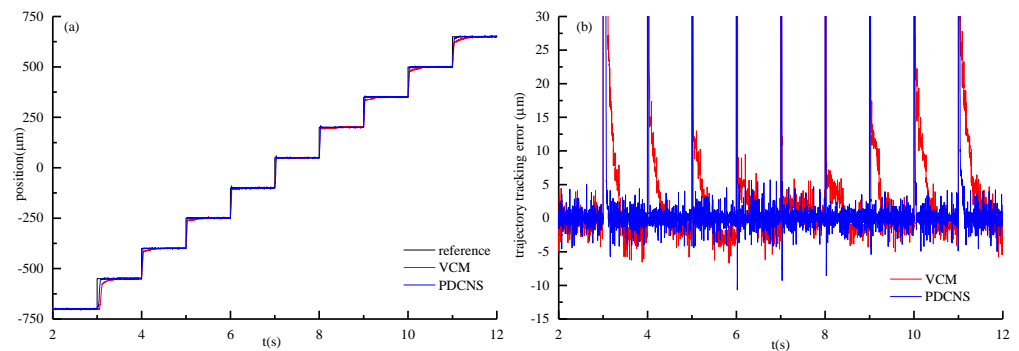


Figure 12. Consecutive-step trajectory (from -0.7 mm to 0.65 mm with a step size of 0.15 mm) control tests (a) tracking results and (b) tracking errors.

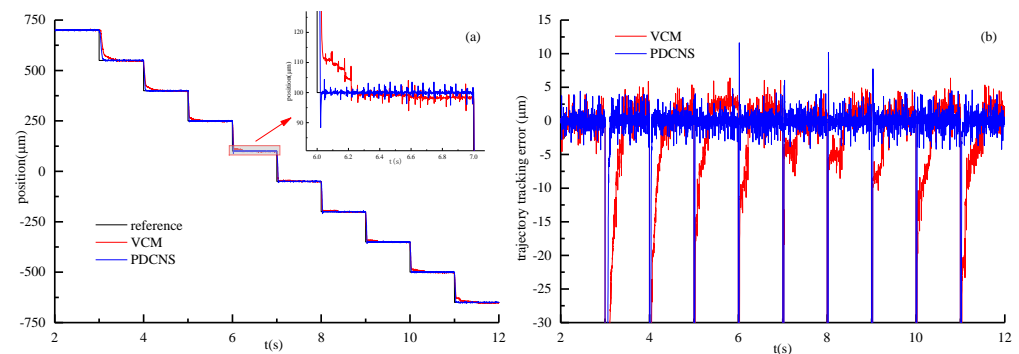


Figure 13. Consecutive-step trajectory (from 0.7 mm to -0.65 mm with a step size of -0.15 mm) control tests (a) tracking results and (b) tracking errors.

(3) Positioning with μm -level steps. To evaluate the precision positioning capability of the proposed PDCNS, consecutive-step-positioning tests with step sizes of $\pm 1 \mu\text{m}$ are performed, as shown in Figures 14 and 15. Compared to the VCM (with PID), faster setting and smaller error can be achieved by the PDCNS (with DSCC). Because severe hysteresis exists in the VCM, it is time consuming for the PID to provide a control signal that can start the motion of the VCM. Due to the existence of friction, it is also a challenging job for the VCM to converge the end effector towards the reference position steadily. Different from the VCM, the PDCNS guarantees the convergence of the tracking error by coordinating the PEA and VCM. The VCM is responsible for driving the end effector close to the reference

position as well as decreasing the control effort of the PEA in a slow manner. Meanwhile, the PEA is in charge of eliminating the tracking error in a fast manner. Therefore, the proposed PDCNS can realize large-range, high-speed, and high-resolution positioning.

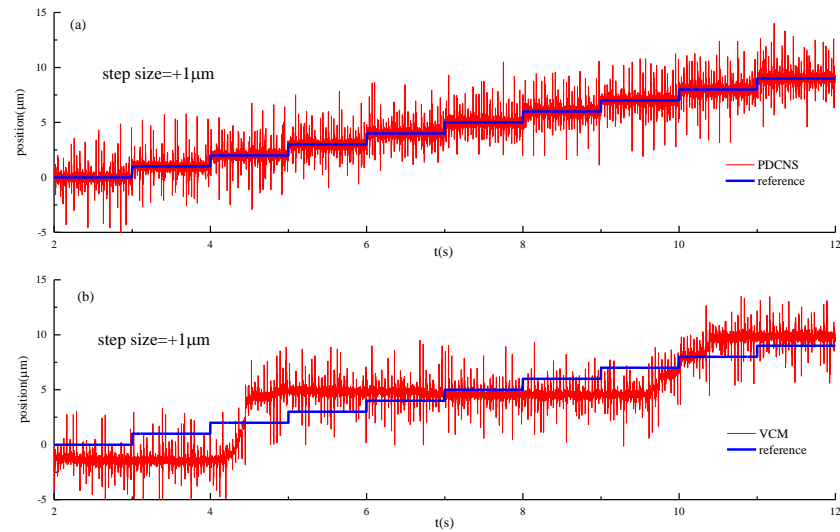


Figure 14. Multistep (step size of $+1\ \mu\text{m}$) response of (a) PDCNS and (b) VCM.

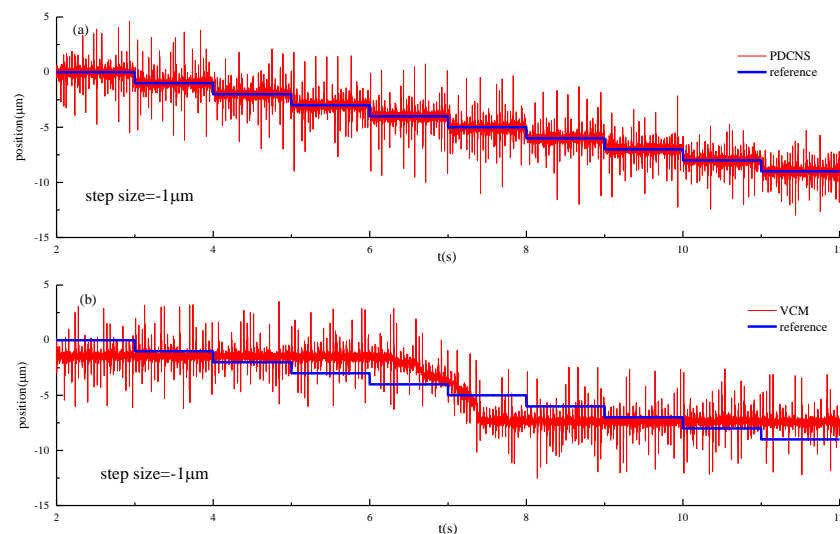


Figure 15. Multistep (step size of $-1\ \mu\text{m}$) response of (a) PDCNS and (b) VCM.

(4) Positioning with nm-level steps. Finally, the nanometer-level positioning capability of the proposed PDCNS (with DSCC) is investigated by two consecutive-step reference signals with step sizes of $\pm 50\ \text{nm}$. In this subsection, to improve the signal-to-noise ratio, the laser displacement sensor is configured to have a measurement range of $-10\ \mu\text{m}$ to $10\ \mu\text{m}$ (corresponding to an output voltage of $-10\ \text{V}$ to $10\ \text{V}$). A $50\ \text{nm}$ height staircase trajectory response is clearly obtained in Figure 16a. Moreover, a continuous stepping movement with amplitude of $-50\ \text{nm}$ can be observed in Figure 16b. Therefore, the closed-loop-positioning resolution of the proposed PDCNS is better than $50\ \text{nm}$.

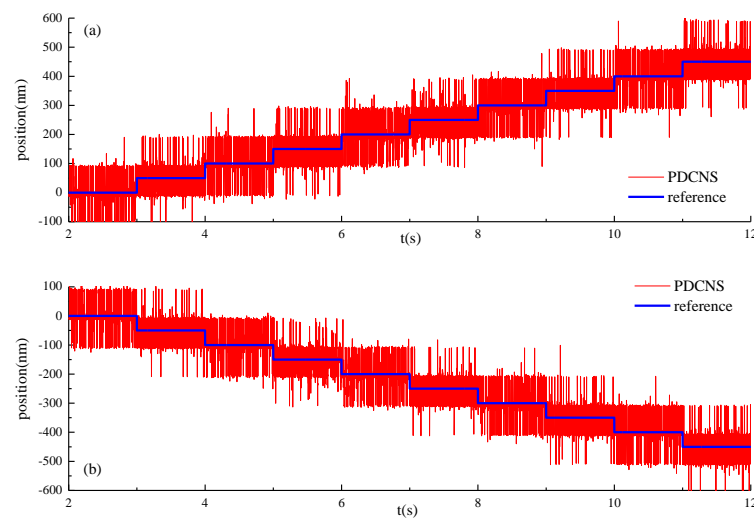


Figure 16. Closed-loop-positioning tests of PDCNS, with step sizes of (a) +50 nm (b) −50 nm.

6. Conclusions

In this paper, the mechanical design, analytical modeling, and closed-loop control of a novel PDCNS are conducted. The designed PDCNS combines the coarse motion from a voice coil motor and the fine motion from a piezoelectric actuator through a new ACPM, which breaks through many barriers encountered in traditional serial dual-stage systems. To resolve the kinematic characteristics of the proposed ACPM, an analytical model is specially established. Furthermore, a DSCC strategy with good robustness to nonlinearities is devised to enhance the positioning capability of the PDCNS.

Simulations and experiments are conducted to demonstrate the static and dynamic performance of the PDCNS. The results show that the maximum stroke of the PDCNS can reach 1.49 mm, and the positioning resolution can be better than 50 nm. Moreover, the designed DSCC can eliminate the steady-state position error of PDCNS, despite many nonlinear factors.

Author Contributions: Conceptualization, X.Y., L.J.; methodology, X.Y., L.J.; validation, X.Y., L.J.; writing—X.Y., Y.S., W.Z., S.L. All authors have read and agreed to the published version of the manuscript.

Funding: This research was funded by the National Key R&D Program of China under Grant 2019YFB2005304, the National Natural Science Foundation of China under Grant 52175018 & 51875505, the Natural Science Foundation of Shandong Province under Grant ZR2020YQ37 & ZR2019QEE023, the Shandong Provincial Key Research and Development Program Major Scientific and Technological Innovation Project: 2019JZZY010802.

Institutional Review Board Statement: Not applicable.

Informed Consent Statement: Not applicable.

Data Availability Statement: Not applicable.

Conflicts of Interest: The authors declare no conflict of interest.

References

1. Nikooienejad, N.; Maroufi, M.; Moheimani, S.O.R. Iterative Learning Control for Video-Rate Atomic Force Microscopy. *IEEE/ASME Trans. Mechatron.* **2021**, *26*, 2127–2138. [\[CrossRef\]](#)
2. Zhu, W.; Yang, X.; Duan, F.; Zhu, Z.; Ju, B. Design and Adaptive Terminal Sliding Mode Control of a Fast Tool Servo System for Diamond Machining of Freeform Surfaces. *IEEE Trans. Ind. Electron.* **2019**, *66*, 4912–4922. [\[CrossRef\]](#)
3. Wan, N.; Wen, J.; Hu, Y.; Kan, J.; Li, J. A Parasitic Type Piezoelectric Actuator with an Asymmetrical Flexure Hinge Mechanism. *Microsyst. Technol.* **2020**, *26*, 917–924. [\[CrossRef\]](#)
4. Wei, Y.; Xu, Q. A Survey of Force-Assisted Robotic Cell Microinjection Technologies. *IEEE Trans. Automat. Sci. Eng.* **2019**, *16*, 931–945. [\[CrossRef\]](#)

5. Chen, X.; Deng, Z.; Hu, S.; Gao, J.; Gao, X. Designing a Novel Model of 2-DOF Large Displacement with a Stepwise Piezoelectric-Actuated Microgripper. *Microsyst. Technol.* **2020**, *26*, 2809–2816. [\[CrossRef\]](#)
6. Eleftheriou, E. Nanopositioning for Storage Applications. *Annu. Rev. Control* **2012**, *36*, 244–254. [\[CrossRef\]](#)
7. Yang, X.; Zhu, W.; Zhu, Z.; Zhu, L. Design, Assessment, and Trajectory Control of a Novel Decoupled Robotic Nanomanipulator. *IEEE/ASME Trans. Mechatron.* **2022**, 1–12. [\[CrossRef\]](#)
8. Yang, X.; Zhu, W.; Zhu, Z.; Zhu, L. Development of a New Compliant Active-Force Support System. *IEEE/ASME Trans. Mechatron.* **2022**, *27*, 372–382. [\[CrossRef\]](#)
9. Tao, Y.; Li, H.; Zhu, L. Time/Space-Separation-Based Gaussian Process Modeling for the Cross-Coupling Effect of a 2-DOF Nanopositioning Stage. *IEEE/ASME Trans. Mechatron.* **2021**, *26*, 2186–2194. [\[CrossRef\]](#)
10. Fleming, A.J.; Aphale, S.; Moheimani, S.O.R. A New Method for Robust Damping and Tracking Control of Scanning Probe Microscope Positioning Stages. *IEEE Trans. Nanotechnol.* **2010**, *9*, 438–448. [\[CrossRef\]](#)
11. Yong, Y.K.; Moheimani, S.O.R.; Kenton, B.J.; Leang, K.K. Invited review article: High-Speed Flexure-Guided Nanopositioning: Mechanical Design and Control Issues. *Rev. Sci. Instrum.* **2012**, *83*, 121101. [\[CrossRef\]](#) [\[PubMed\]](#)
12. Tan, K.K.; Lee, T.H.; Zhou, H.X. Micro-Positioning of Linear-Piezoelectric Motors Based on a Learning Nonlinear PID Controller. *IEEE/ASME Trans. Mechatron.* **2001**, *6*, 428–436. [\[CrossRef\]](#)
13. Ho, S.T.; Jan, S.J. A Piezoelectric Motor for Precision Positioning Applications. *Precis. Eng.* **2016**, *43*, 285–293. [\[CrossRef\]](#)
14. Li, J.P.; Huang, H.; Morita, T. Stepping Piezoelectric Actuators with Large Working Stroke for Nano-positioning Systems: A Review. *Sens. Actuators A Phys.* **2019**, *292*, 39–51. [\[CrossRef\]](#)
15. Delibas, B.; Koc, B. A Method to Realize Low Velocity Movability and Eliminate Friction Induced Noise in Piezoelectric Ultrasonic Motors. *IEEE/ASME Trans. Mechatron.* **2020**, *25*, 2677–2687. [\[CrossRef\]](#)
16. Mamun, A.A.; Mareels, I.; Lee, T.H.; Tay, A. Dual Stage Actuator Control in Hard Disk Drive—A review. In Proceedings of the Industrial Electronics Conference, Roanoke, VA, USA, 2–6 November 2003.
17. Zhu, Z.; Du, H.; Zhou, R.; Huang, P.; Zhu, W.; Guo, P. Design and Trajectory Tracking of a Nanometric Ultra-Fast Tool Servo. *IEEE Trans. Ind. Electron.* **2020**, *67*, 432–441. [\[CrossRef\]](#)
18. Gutierrez, H.M.; Ro, P.I. Sliding-Mode Control of a Nonlinear-Input System: Application to a Magnetically Levitated Fast-Tool Servo. *IEEE Trans. Ind. Electron.* **1998**, *45*, 921–927. [\[CrossRef\]](#)
19. Yang, X.; Zhu, W. Design, Analysis and Test of a Novel Self-Sensing Fast Tool Servo. *IEEE Trans. Ind. Informat.* **2020**, *16*, 4447–4455. [\[CrossRef\]](#)
20. Wang, G.; Xu, Q. Design and Precision Position/Force Control of a Piezo-Driven Microinjection System. *IEEE/ASME Trans. Mechatron.* **2017**, *22*, 1744–1754. [\[CrossRef\]](#)
21. Permana, S.; Grant, E.; Walker, G.M.; Yoder, J.A. A Review of Automated Microinjection Systems for Single Cells in the Embryogenesis Stage. *IEEE/ASME Trans. Mechatron.* **2016**, *21*, 2391–2404. [\[CrossRef\]](#)
22. Xu, Q. Design and Development of Flexure-Based Dual-Stage Nanopositioning System with Minimum Interference Behavior. *IEEE Trans. Autom. Sci. Eng.* **2012**, *9*, 554–563. [\[CrossRef\]](#)
23. Michellod, Y.; Mullhaupt, P.; Gillet, D. Strategy for the Control of a Dual-Stage Nano-Positioning System with a Single Metrology. In Proceedings of the 2006 IEEE Conference on Robotics, Automation and Mechatronics, Bangkok, Thailand, 1–3 June 2006; pp. 1–8.
24. Dong, W.; Tang, J.; ElDeeb, Y. Design of a Linear-Motion Dual-Stage Actuation System for Precision Control. *Smart Mater. Struct.* **2009**, *18*, 095035. [\[CrossRef\]](#)
25. Zhu, H.; Pang, C.K.; Teo, T.J. Integrated Servo-Mechanical Design of a Fine Stage for a Coarse/Fine Dual-Stage Positioning System. *IEEE/ASME Trans. Mechatron.* **2016**, *21*, 329–338. [\[CrossRef\]](#)
26. Long, Y.Q.; Bao, S.H.; Yuan, S. *Structural Mechanics*, 3rd ed.; The Higher Education Press: Beijing, China, 2012.
27. Zhu, W.; Zhu, Z.; Shi, Y.; Wang, X.; Guan, K.; Ju, B. Design, Modeling, Analysis and Testing of a Novel Piezo-Actuated XY Compliant Mechanism for Large Workspace Nano-Positioning. *Smart Mater. Struct.* **2016**, *25*, 115033. [\[CrossRef\]](#)
28. Koseki, Y.; Tanikawa, T.; Koyachi, N.; Arai, T. Kinematic Analysis of Translational 3-DOF Micro Parallel Mechanism Using Matrix Method. In Proceedings of the 2000 IEEE/RSJ International Conference on Intelligent Robots and Systems, Takamatsu, Japan, 31 October–5 November 2000; pp. 786–792.
29. Ling, M.; Cao, J.; Li, Q.; Zhuang, J. Design, Pseudo-Static Model and PVDF-Based Motion Sensing of a Piezo-Actuated XYZ Flexure Manipulator. *IEEE/ASME Trans. Mechatron.* **2018**, *23*, 2837–2848. [\[CrossRef\]](#)
30. Zhu, W.; Zhu, Z.; To, S.; Liu, Q.; Ju, B.; Zhou, X. Redundantly Piezo-Actuated XYθz Compliant Mechanism for Nano-Positioning Featuring Simple Kinematics, Bi-Directional Motion and Enlarged Workspace. *Smart Mater. Struct.* **2016**, *25*, 125002. [\[CrossRef\]](#)
31. Guo, Z.; Tian, Y.; Liu, C.; Wang, F.; Liu, X.; Shirinzadeh, B.; Zhang, D. Design and Control Methodology of a 3-DOF Flexure-Based mechanism for Micro/Nano Positioning. *Robot. Comput-Integr. Manuf.* **2015**, *32*, 93–105. [\[CrossRef\]](#)
32. Chen, M. Research on Mechanical Properties Test and Dynamic Material Model of TC4 Titanium Alloy. Master's Thesis, Nanjing University of Aeronautics and Astronautics, Nanjing, China, 2012.
33. Wang, D.; Yang, Q.; Dong, H. A Monolithic Compliant Piezoelectric-Driven Microgripper: Design, Modeling, and Testing. *IEEE/ASME Trans. Mechatron.* **2013**, *18*, 138–147. [\[CrossRef\]](#)